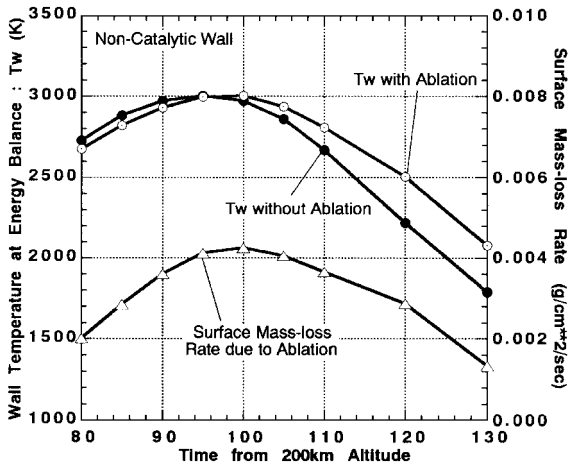

Fig. 4 Time history of wall temperature and surface mass loss rate.

because the wall temperature remains in the diffusion-controlled regime through the trajectory, and the surface oxidation reaction results in heat release to the flow near the surface. When the wall temperature reaches the sublimation regime, the convective heating rate is significantly reduced.[2] In the flight regime of peak stagnation heating, the heat flux augmentation due to the surface oxidation is much smaller than that due to the catalytic recombination. However, the difference becomes smaller at lower altitudes. The temporal variations of the wall temperature and the surface mass loss rate along the trajectory are presented in Fig. 4. After the peak convective heating, the surface mass loss rate decreases gradually because it is not sensitive to the wall temperature in the diffusion-controlled regime, as shown in Fig. 1. Consequently, the wall temperature for the ablating wall becomes higher than that for the nonablating wall at lower altitude.

Concluding Remarks

The ablation phenomena are formulated in a framework of the nonequilibrium chemistry of the 19 carbon–oxygen–nitrogen species. The boundary conditions at the ablating surface for the shock-layer flow computation are presented by considering the finite rate surface reactions of catalytic recombination, ion–electron recombination, surface oxidation, and sublimation. Results of the VSL analysis demonstrate that both the diffusion-controlled regime and sublimation regime are successfully described by the present analysis model. This method is applied to the trajectory-based analysis of the stagnation-point aerodynamic heating environment of the superorbital re-entry capsule for the MUSES-C asteroid sample return mission.

References

[1]Working Group of Asteroid Sample Return Mission, "MUSES-C Mission Plan Report," Inst. of Space and Astronautical Science, Kanagawa, Japan, March 1995 (in Japanese).

[2]Suzuki, K., Kubota, H., Fujita, K., and Abe, T., "Chemical Nonequilibrium Ablation Analysis of Muses-C Super-Orbital Reentry Capsule," AIAA Paper 97-2481, June 1997.

[3]Gupta, R. N., and Simmonds, A. L., "Stagnation Flowfield Analysis for an Aeroassist Flight Experiment Vehicle," AIAA Paper 88-2613, June 1988.

[4]Blottner, F. G., "Prediction of Electron Density in the Boundary Layer on Entry Vehicles with Ablation," NASA SP-252, Oct. 1970, pp. 219–240.

[5]Ahn, H. K., and Park, C., "Preliminary Study of the MUSES-C Reentry," AIAA Paper 97-0278, Jan. 1997.

[6]Park, C., "Effects of Atomic Oxygen on Graphite Ablation," *AIAA Journal*, Vol. 14, No. 11, 1976, pp. 1640–1642.

[7]Metzger, J. W., Engel, M. J., and Diaconis, N. S., "Oxidation and Sublimation of Graphite in Simulated Re-Entry Environments," *AIAA Journal*, Vol. 5, No. 5, 1967, pp. 451–460.

T. C. Lin
Associate Editor

Truss Structure Effects on International Space Station Global Positioning System Antenna Performance

Shian U. Hwu*
Lockheed Martin Space Mission Systems and Services, Houston, Texas 77258
and
Robert J. Panneton†
NASA Johnson Space Center, Houston, Texas 77258

Introduction

THE International Space Station (ISS) will use the Global Positioning System (GPS) for providing position, velocity, attitude determination, and time reference. The choke-ring GPS antennas are located on the center truss segment (SO truss segment) of the Space Station as shown in Fig. 1. There are concerns about the multipath effects (signal interference due to reflections and diffractions) of the SO truss structure on the GPS antenna gain and phase patterns. Multipath from the SO truss and surrounding objects may degrade the accuracy of the GPS performance.[1] To investigate the SO truss effects on the space station GPS antenna gain and phase patterns, three different configurations of the truss structures were analyzed. A series of tests of the GPS antenna on the SO truss was performed using the NASA Johnson Space Center radio frequency anechoic chamber antenna test facilities for comparison of both GPS antenna gain and phase patterns. Computational investigations were also performed using the electromagnetic modeling technique. The uniform geometrical theory of diffraction (UTD) was applied to compute the GPS antenna gain and phase patterns including multipath effects from the three different truss configurations.[2,3] Measured and computed data were analyzed and compared for the different truss configurations.

Experimental Investigations

The four tested configurations, as shown in Fig. 1, are as follows: 1) free space configuration—GPS antenna only (no truss structures), 2) truss configuration 1—antenna on SO truss (no boxes and no cable trays), 3) truss configuration 2—antenna on SO truss with boxes and cable trays, and 4) truss configuration 3—antenna on SO truss, which is covered with metal sheet.

The measured GPS antenna gain and phase patterns are presented and compared in Figs. 2 and 3. Test results indicate the three investigated truss configurations only slightly affected the upper-hemisphere portion of the GPS patterns. By upper-hemisphere portion, one means the region where the GPS satellites are to be found (±90 deg from antenna boresight). Measured data show little difference between a GPS antenna on an open truss with boxes (truss configurations 1 and 2) or a solid truss (truss configuration 3). The choke-ring GPS antenna consists of several concentric metallic circular fins on a ground plane, as shown in Fig. 1. The choke-ring feature may reduce the signal interference from the truss structures.[4] The various truss structures mainly affected the GPS antenna patterns in the lower-hemisphere portion (±90–±180 deg from antenna boresight). Because the GPS antennas track the GPS satellites in the upper hemisphere, the truss structures should not affect ISS GPS antenna performance significantly.

Received Sept. 2, 1997; revision received Feb. 23, 1998; accepted for publication Feb. 28, 1998.

*Advanced Systems Engineering Specialist, Communication Systems Analysis and Test Section, 2400 NASA Road 1. Senior Member AIAA.
†Chief Engineer, Avionics Test and Analysis Branch, MC: EV413.

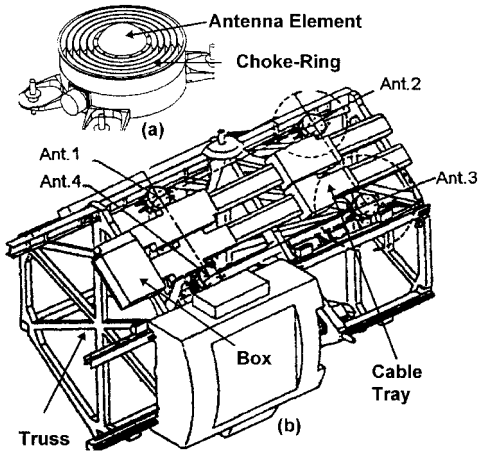

Fig. 1 a) GPS antenna and b) SO truss segment.

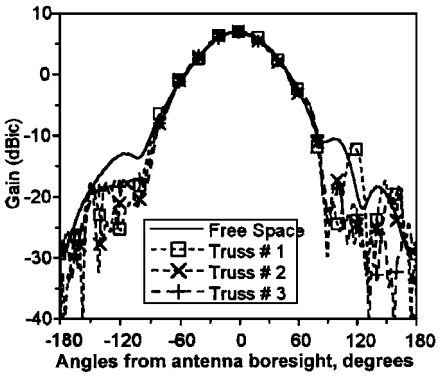

Fig. 2 Comparison of measured gain patterns.

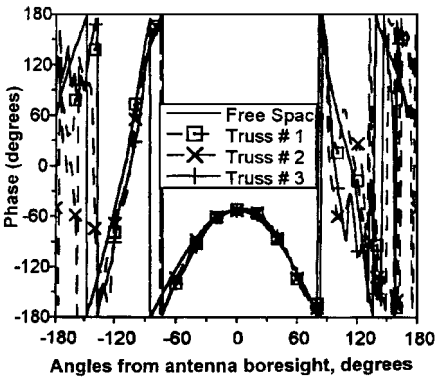

Fig. 3 Comparison of measured phase patterns.

Computational Investigations

Computational investigations were performed using the electromagnetic modeling technique. The UTD technique was applied to model and to compute the GPS antenna patterns with different SO truss configurations. The UTD technique provides a high-frequency approximate solution to the electromagnetic fields—including incident, reflected, and diffracted fields—and their interactions.[2] In the field computation, the incident, reflected, and diffracted fields are determined by the field incident on the reflection or diffraction point multiplied by a dyadic reflection or diffraction coefficient, a spreading factor, and a phase term.[2] The reflected and diffracted fields at a field point r', $\boldsymbol{E}^{r,d}(r')$, in general have the following form:

$$\boldsymbol{E}^{r,d}(r') = \boldsymbol{E}^{i}(r)\boldsymbol{D}^{r,d}\boldsymbol{A}^{r,d}(s)e^{-jks} \tag{1}$$

where $\boldsymbol{E}^{i}(r)$ is the field incident on the reflection or diffraction point r, $\boldsymbol{D}^{r,d}$ is a dyadic reflection or diffraction coefficient, $\boldsymbol{A}^{r,d}(s)$ is a spreading factor, and s is the distance from the reflection or diffraction point r to the field point r'. The terms $\boldsymbol{D}^{r,d}$ and $\boldsymbol{A}^{r,d}$ can be found from the geometry of the structure at reflection or diffraction point r and the properties of the incident wave there.

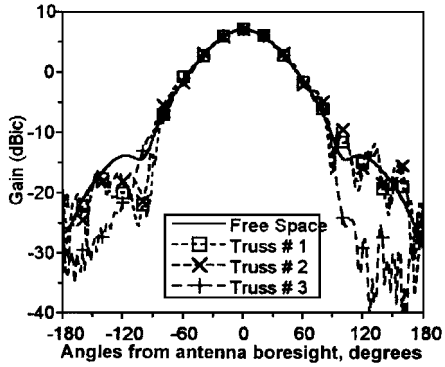

Fig. 4 Comparison of computed gain patterns.

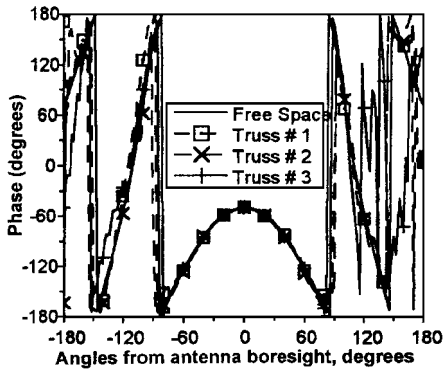

Fig. 5 Comparison of computed phase patterns.

The application of UTD to a given radiation problem is first to decompose the scattering structure into simple geometrical shapes, given that the reflection and diffraction coefficients for them are known. Next, all field components contributing to the radiation intensity in the field point must be traced, and the individual contributions must be determined.[2] The resultant field is given by summing all of the complex contributing components:

$$E^{\text{tot}} = E^{\text{inc}} + \sum_{n=1}^{N} E_n^{\text{ref}} + \sum_{m=1}^{M} E_m^{\text{dif}} \tag{2}$$

where E^{tot} is the total field at the observation point, E^{inc} is the direct incident fields from antenna, E^{ref} is the reflected field from plates and cylinders, and E^{dif} is the diffracted field from plates and cylinders. Detailed information on the theory of this method can be found in Refs. 2 and 3.

Figures 4 and 5 show the UTD-computed GPS antenna gain and phase patterns for free space (no truss) and three different tested truss configurations. By comparison with the free space antenna patterns, the computed antenna patterns, including multipath from the truss structures, are changed mainly in the lower-hemisphere portion. The truss structures do not affect the GPS patterns much in the upper-hemisphere portion. The truss structures cause only small ripples that are present in the upper-hemisphere portion of the gain and phase patterns. This agrees with observations from previous experimental test results.

Conclusions

Both test and computed results indicate that the truss structures do not have much effect on the upper-hemisphere portion of the GPS antenna patterns. The truss structures mainly affect the GPS antenna patterns in the lower-hemisphere portion. Note that the choke-ring of the GPS antenna is designed to minimize the multipath effects in the low-elevation angles. The choke-ring may reduce the signal interference from the truss structures. Both measured and computed

data indicate that the multipath effects from the SO truss segment should not be of concern to the ISS GPS antenna performance.

References

[1]Cohen, C. E., "Attitude Determination Using GPS," Ph.D. Dissertation, Dept. of Aeronautics and Astronautics, Stanford Univ., Stanford, CA, Dec. 1992.

[2]Marhefka, R. J., and Silvestro, J. W., "Near Zone—Basic Scattering Code User's Manual with Space Station Applications," NASA CR-181944, Dec. 1989.

[3]Gomez, S. F., Panneton, R. J., Saunders, P. E., Hwu, S. U., and Lu, B. P., "GPS Multipath Modeling and Verification Using Geometrical Theory of Diffraction," *Proceedings of ION GPS-95*, Inst. of Navigation, Alexandria, VA, 1995, pp. 195–204.

[4]Tranquilla, J. M., Carr, J. P., and Al-Rizzo, H. M., "Analysis of a Choke-Ring Groundplane for Multipath Control in Global Positioning System (GPS) Applications," *IEEE Transactions on Antennas and Propagation*, Vol. 42, No. 7, 1994, pp. 905–911.

R. B. Malla
Associate Editor

Mercury Mission Design Using Solar Electric Propulsion Spacecraft

Craig A. Kluever* and Mudar Abu-Saymeh†
University of Missouri–Columbia/Kansas City, Kansas City, Missouri 64110-2499

Introduction

THE advantages of using low-thrust electric propulsion (EP) for interplanetary missions that require a large energy change have been documented.[1] Several studies have demonstrated the payload enhancements associated with utilizing EP for transfers to the outer planets. For example, previous mission studies include a manned Mars mission[2] and scientific missions to Jupiter, Uranus, Neptune, and Pluto.[3,4] In addition, the first New Millennium mission will use solar electric propulsion (SEP) as the primary propulsion mode for transferring a spacecraft to an asteroid.[5] However, few mission studies have investigated the use of EP for transfers to the inner planets, and, to our knowledge, no research involving a low-thrust rendezvous with Mercury using SEP has ever been published.

In this Note, the feasibility of using SEP for a Mercury mission is investigated by computing the optimal orbit transfers that maximize the spacecraft payload mass at Mercury rendezvous. The proposed Mercury rendezvous is a Discovery-class mission that utilizes Delta and Med-lite launch vehicles for injection into heliocentric space. The EP system consists of 30-cm ion thrusters that are similar to the proposed thrusters for the first New Millennium mission.[5] For this analysis, the orbit transfer is governed by two-body dynamics, and a gravity assist from Venus is included to reduce further the orbital energy enroute to the Mercury rendezvous. Numerical results are presented for maximum payload trajectories.

Spacecraft System Analysis

The payload mass can be computed as the net mass m_{net}, which is defined as

$$m_{\text{net}} = m_0 - m_{\text{prop}} - m_{\text{tank}} - m_{\text{pp}} \tag{1}$$

where m_0 is the injected mass into heliocentric space, m_{prop} is the total SEP propellant mass, m_{tank} is the tank mass, and m_{pp} is the SEP power- and propulsion-system mass. The spacecraft's net mass represents the usable mass for payload plus the basic spacecraft structural mass, which includes "housekeeping" functions such as communication and thermal protection. The basic structural mass can be computed[2] as a percentage (5–10%) of the initial mass m_0. Injected mass m_0 is computed via launch performance curves for the Delta and Med-lite vehicles with launch energy C_3 as the independent variable. The tank mass m_{tank} is assumed to be 15% of the propellant mass m_{prop}, and the power- and propulsion-system mass m_{pp} is a function of the input power at 1 AU (P_0) and specific mass (α). The parameter α is fixed at 35 kg/kW for this analysis, which represents the near-term SEP technology level.[6]

It is assumed that xenon is utilized as the propellant for the EP system and that thruster efficiency η is 66% and specific impulse I_{sp} is 3360 s, which corresponds to the SEP system for the first New Millennium mission.[5] Furthermore, it is assumed that I_{sp} is constant over the entire mission, which implies a fixed engine operating point with no throttling. For our preliminary analysis, the input power P for the SEP spacecraft is assumed to behave in an inverse-square relation with radial distance from the sun. Because the orbit transfer is to an inner planet, P increases as radial distance decreases. Furthermore, we assume that power reaches a maximum value of $2P_0$ and that this maximum power level can be maintained by controlling the attitude of the solar arrays when the radial distance is less than 0.7071 AU.

Trajectory Optimization

The objective of the Mercury mission design is to maximize the net mass of the spacecraft at Mercury rendezvous conditions. We assume a fixed heliocentric trajectory sequence that begins with a powered SEP arc near the Earth's sphere of influence (SOI) after chemical injection into heliocentric space followed by a coasting phase that includes a Venus gravity assist and finally a second powered SEP arc to Mercury rendezvous. The insertion into a parking orbit about Mercury is not addressed in this study. The trajectory design variables include the launch date, the hyperbolic velocity vector at the SOI, the durations of the two powered arcs, the thrust direction for the powered arcs, the changes in true longitude for the coast arcs, the planetary flyby conditions, and the rendezvous date. The trajectory is governed by the equations of motion for a thrusting spacecraft in an inverse-square gravitational field. The powered arcs are numerically computed by integrating the equations of motion using a fixed-step, fourth-order Runge–Kutta routine with 100 integration steps for the first powered arc and 500 steps for the second arc. The coast arcs are computed analytically using two-body mechanics. Planetary gravity assists are modeled as instantaneous changes in velocity ΔV without change in spacecraft position. The gravity assist is defined by two free parameters: the periapsis radius and orbit plane orientation for the flyby. Details of the numerical simulation of the trajectory are presented in Ref. 7.

Numerical solutions of the trajectory optimization problem are obtained by utilizing sequential quadratic programming (SQP), a constrained parameter optimization method.[8] The SQP code used here is taken from Ref. 9 and computes the gradients with forward finite differences. The thrust steering history is defined by three direction cosines, which are parameterized in the optimization problem by linear interpolation through a set of control nodes. Nine SQP equality constraints are imposed: Six constraints maintain the match between the orbital elements of the spacecraft and Mercury at the final end time, and three constraints maintain the match between the position of the spacecraft and Venus at the gravity assist. The planetary elements are computed by a solar system ephemeris.

Results

Maximum Payload Trajectories

Several trajectories maximizing m_{net} are obtained for a range of input power levels P_0, and the results are shown in Fig. 1. Although the launch date is a free design variable, we chose a nominal launch date in the mid-2002 time frame. Optimal transfers are obtained for

Presented as Paper 97-173 at the AAS/AIAA Space Flight Mechanics Meeting, Huntsville, AL, Feb. 10–12, 1997; received Nov. 13, 1997; revision received Feb. 24, 1998; accepted for publication Feb. 24, 1998.

*Assistant Professor, Mechanical and Aerospace Engineering Department. Member AIAA.

†Graduate Research Assistant, Mechanical and Aerospace Engineering Department.